

# CT substitute derived from MRI sequences with ultrashort echo time

Adam Johansson,<sup>a)</sup> Mikael Karlsson, and Tufve Nyholm  
*Department of Radiation Sciences, Umeå University, Umeå, Sweden*

(Received 26 January 2011; revised 28 March 2011; accepted for publication 28 March 2011;  
published 9 May 2011)

**Purpose:** Methods for deriving computed tomography (CT) equivalent information from MRI are needed for attenuation correction in PET/MRI applications, as well as for patient positioning and dose planning in MRI based radiation therapy workflows. This study presents a method for generating a drop in substitute for a CT image from a set of magnetic resonance (MR) images.

**Methods:** A Gaussian mixture regression model was used to link the voxel values in CT images to the voxel values in images from three MRI sequences: one T2 weighted 3D spin echo based sequence and two dual echo ultrashort echo time MRI sequences with different echo times and flip angles. The method used a training set of matched MR and CT data that after training was able to predict a substitute CT (s-CT) based entirely on the MR information for a new patient. Method validation was achieved using datasets covering the heads of five patients and applying leave-one-out cross-validation (LOOCV). During LOOCV, the model was estimated from the MR and CT data of four patients (training set) and applied to the MR data of the remaining patient (validation set) to generate an s-CT image. This procedure was repeated for all five training and validation data combinations.

**Results:** The mean absolute error for the CT number in the s-CT images was 137 HU. No large differences in method accuracy were noted for the different patients, indicating a robust method. The largest errors in the s-CT images were found at air–tissue and bone–tissue interfaces. The model accurately discriminated between air and bone, as well as between soft tissues and nonsoft tissues.

**Conclusions:** The s-CT method has the potential to provide an accurate estimation of CT information without risk of geometrical inaccuracies as the model is voxel based. Therefore, s-CT images could be well suited as alternatives to CT images for dose planning in radiotherapy and attenuation correction in PET/MRI. © 2011 American Association of Physicists in Medicine.

[DOI: 10.1118/1.3578928]

Key words: magnetic resonance imaging, computed tomography substitute, ultrashort echo time, Gaussian mixture, dose calculation

## I. INTRODUCTION

Intensity in computed tomography (CT) images is directly related to electron density. Therefore, CT is used for attenuation correction of SPECT and PET images and as a basis for dose calculations in external radiotherapy. Also, digitally reconstructed radiographs derived from CT images are used for patient positioning in radiotherapy. However, interest is emerging in replacing information from CT images with magnetic resonance (MR) information for attenuation correction, dose planning, and patient positioning for integration of PET and MR modalities into a combined PET/MR scanner<sup>1</sup> and to derive the benefits of fully MR driven radiotherapy workflows.<sup>2–5</sup> The feasibility of MR based dose planning has been demonstrated for radiotherapy of different treatment regions using manual segmentation and bulk density assignment<sup>2,6</sup> while automatic methods have been evaluated for attenuation corrections of PET images.<sup>7–11</sup>

Two families of algorithms for transformation of MR data to CT like data exist: anatomy and voxel based methods. Anatomy based methods use deformable image registration between a reference MR image and a new patient's MR image to warp a reference CT image to match the anatomy

of the new patient. The main drawback of this method is uncertainty in image registration for patients with atypical anatomy.<sup>7,9</sup> Voxel based methods avoid dependence on image registration by direct characterization of individual voxels into different tissue classes, followed by bulk assignment of electron densities,<sup>7,8</sup> or direct conversion of MR voxel values to Hounsfield units (HU) or electron density.<sup>9</sup> The main challenge for voxel based methods is the extremely short T2 relaxation time of bone, 0.4–0.5 ms, which makes separation of bone and air difficult or even impossible with traditional MR sequences. Therefore, ultrashort echo time (UTE) sequences are used to acquire signal from cortical bone. UTE sequences sample the free induction decay (FID) rather than a spin or gradient echo.<sup>12,13</sup>

Derivation of attenuation maps for PET using UTE sequences with two different echo times by segmenting the images into air, soft tissues, and bone has recently been reported.<sup>7,8</sup> The idea with the dual echo sequence is to characterize the tissue in a specific voxel based on T2. However, because UTE sequences sample either the FID or a gradient echo, the contrast in the images is controlled by T2\* rather than T2.<sup>12,13</sup> Therefore, the dual echo approach leads to difficulties in distinguishing voxels with a short T2, such as

cortical bone, from those with a long T2 combined with a short T2\*, for example, interfaces between air and soft tissues in the concha and sinuses.

In this study, a voxel based method for generating a substitute CT (s-CT) image based on MRI data with improved performance in regions with interfaces between different tissue types was developed. The method was based on a Gaussian mixture regression model<sup>14,15</sup> linking intensities in reference MR images (two dual echo UTE images with different flip angles and one high resolution T2 weighted image) to HU in reference CT images. The derived model was used to transform a set of MR images into an s-CT image. The algorithm was evaluated using retrospective analysis of clinical imaging data for five radiotherapy patients using leave-one-out cross-validation (LOOCV).

## II. MATERIALS AND METHODS

Five datasets of matched MRI and CT data from the head region were used.

### II.A. MR imaging

All five patients were scanned with three sequences—two dual echo UTE sequences with different flip angles and one T2 weighted 3D spin echo based sequence (SPACE).

The UTE sequences sampled a first echo (FID) with an echo time of 0.07 ms and a second echo (gradient echo) with an echo time of 3.76 ms, both from the same excitation. The same spoke of  $k$ -space was acquired for both echoes to reduce the motion induced difference between the images that were reconstructed from each echo. The first echo time was defined as the delay from the center of the excitation block pulse to the beginning of the FID sampling. The flip angles of the two dual echo UTE sequences were 10° and 60°, respectively. These two UTE sequences generated four images and were selected to distinguish between voxels with a short and long T2\* as well as between voxels with the same short T2\* but a different T1. The repetition time was 6 ms for both sequences. The UTE images were reconstructed to a  $192 \times 192 \times 192$  matrix. The matrix had isotropic resolution and a voxel size of 1.33 mm.  $k$ -space was sampled in 30 000 radial spokes. The scan time was 3 min for each dual echo sequence.

Since the UTE sequence collected only a single radial spoke of  $k$ -space per excitation, a short repetition time was needed for the sequence to run in under a few minutes. This short repetition time led to a loss of signal in tissues with a long T1, such as the cerebrospinal fluid and the vitreous body in the eye. To enable separation between tissues with a long T1 and air, a T2 weighted 3D SPACE was included in the model. The voxel size of the SPACE images was  $0.78 \times 0.78 \times 1.7$  mm<sup>3</sup>. Images were acquired using an echo time of 100 ms, a repetition time of 1500 ms, a 150° flip angle, and a scan time of 5 min.

MR images were corrected for geometrical distortions using a 3D algorithm supplied by Siemens.<sup>16,17</sup> A low resolution prescan was used to correct images for inhomogeneous coil-sensitivity. All images were acquired on a Siemens

Espreo 1.5 T MR scanner using a standard four segment head coil. The total scan time per patient was 11 min.

### II.B. CT imaging

CT images were acquired using a GE Lightspeed with a 2.5 mm slice thickness and reconstructed with an in-plane resolution of  $0.78 \times 0.78$  mm<sup>2</sup>. Tube voltage was 130 kV. As the CT scans were a part of clinical preparation for radiotherapy, the patients were in full radiotherapy fixation when scanned in the CT. Mask fixation was used on three patients (patients 1–3) and bite block fixation on two (patients 4 and 5).

### II.C. Image registration

For each patient, all MR images and the CT image were coregistered using a mutual information algorithm from the Insight Toolkit (ITK).<sup>18</sup> No special treatment of the fixations seen in the CT images was made during registration. Each registration passed a manual evaluation of the registration accuracy. The SPACE image and the CT image were resampled to the same resolution as the UTE images using linear interpolation.

### II.D. Masking

To reduce the computational burden during regression analysis, a binary mask covering the imaged subject was created. This was achieved by first segmenting the short echo UTE image with 10° flip angle into a low and a high intensity segment using Otsu thresholding.<sup>19</sup> The low intensity segment was then morphologically eroded by a seven voxel spherical kernel and the largest connected component was classified as surrounding air. The large erosion kernel ensured that no part of the subject's surface was excluded from the calculation. To eliminate any objects not physically part of the subject, a connected component analysis on the nonair class was done and the largest component was classified as the imaged subject. The fixations present in the CT images were excluded using thresholding. The generated mask determined which voxels were used for the parameter estimation in the regression model.

### II.E. Regression model parameter estimation

A Gaussian mixture regression (GMR) model was defined linking the MR and CT image intensities of the reference dataset. Each image type (five MRI and one CT) was considered a stochastic variable and each voxel intensity a sample of that variable. In addition, for each MR image two new images were derived by calculating the mean value and standard deviation of the voxels in a 27-voxel neighborhood around each voxel. These filtered images increased the total number of variables,  $k$ , to 16. Each voxel was thus characterized by the observations,  $\mathbf{x}$ , of the 16 stochastic variables  $\mathbf{X} = (X_1, \dots, X_k)^T$ , where  $X_1$  is the CT number from the CT image.

The distribution of voxels,  $f_{\mathbf{X}}(\mathbf{x})$ , in this 16-dimensional intensity space was approximated by a mixture of 20 multivariate Gaussians,

$$f_{\mathbf{x}}(\mathbf{x}) = \sum_{i=1}^N a_i g_i(\mathbf{x}), \quad (1)$$

with

$$g_i(\mathbf{x}) = \frac{1}{(2\pi)^{k/2} |\Sigma_i|^{1/2}} \exp\left(-\frac{1}{2}(\mathbf{x} - \boldsymbol{\mu}_i)^T \Sigma_i^{-1} (\mathbf{x} - \boldsymbol{\mu}_i)\right) \quad (2)$$

where  $N$  is the number of Gaussians. The expectation maximization (EM) algorithm was used with  $k$ -means initialization<sup>15</sup> to estimate the mixing proportions,  $a_i$ , mean values,  $\boldsymbol{\mu}_i$ , and covariance matrices,  $\Sigma_i$ .

Because no relation between CT number and MRI intensities can be derived from the physics of x-ray interaction and nuclear magnetic resonance, it is difficult to motivate a particular shape of a regression function. This problem is circumvented in GMR by modeling the joint distribution of the intensities in the CT and MR images. The underlying assumption is then that the images show a discrete number of tissues or clusters. Each cluster is characterized by an intensity value for each image and thereby by a coordinate in the multidimensional intensity space. Because of noise in the images and because of small variations in the appearance of a tissue type, the samples from a particular tissue will fall in a distribution around the tissues types coordinate. This distribution is approximated by a single multivariate Gaussian. The mean value,  $\boldsymbol{\mu}_i$ , then corresponds to the tissue coordinate in the intensity space, the mixing proportion,  $a_i$ , to the tissue's relative frequency in the image and the covariance matrix,  $\Sigma_i$ , to the width of tissue's intensity distribution. Whereas some tissues (e.g., gray and white matter) will have very narrow distribution, others (e.g., bone) will have broader. This information about distribution width along with possible correlations between deviations in CT and MRI images from  $\boldsymbol{\mu}_i$  is also encapsulated in the covariance matrices. Essentially, GMR performs clustering on the whole dataset with voxels from all tissues and then characterizes the dependence between the different variables through the covariance matrix for each cluster.

## II.F. Applying a model on a new dataset

The s-CT for a new patient was generated by calculating the expectation value of the CT number conditional upon the 15 observed MR variables for each voxel. For a distribution consisting of a Gaussian mixture, the expectation value can be given in a closed form expression.<sup>14,15</sup>

Let the first variable  $\mathbf{X}_1 = X_1$  be the CT intensity and  $\mathbf{X}_2 = (X_2, \dots, X_k)^T$  the intensities in the MR images and their filtered counterparts. The expectation of the CT intensity,  $\mathbf{X}_1$ , in a voxel conditional on the observed MR intensities  $\mathbf{X}_2 = \mathbf{x}_2$  in the same voxel is then given by

$$(\mathbf{X}_1 | \mathbf{X}_2 = \mathbf{x}_2) = \frac{\sum_{i=1}^N \bar{\boldsymbol{\mu}}_{1,i} a_i h_i(\mathbf{x}_2)}{\sum_{i=1}^N a_i h_i(\mathbf{x}_2)}, \quad (3)$$

where

$$\bar{\boldsymbol{\mu}}_{1,i} = \boldsymbol{\mu}_{1,i} + \Sigma_{12,i} \Sigma_{22,i}^{-1} (\mathbf{x}_2 - \boldsymbol{\mu}_{2,i}) \quad (4)$$

and

$$h_i(\mathbf{x}_2) = \frac{1}{(2\pi)^{k/2} |\Sigma_{22,i}|^{1/2}} e^{-\frac{1}{2}(\mathbf{x}_2 - \boldsymbol{\mu}_{2,i})^T \Sigma_{22,i}^{-1} (\mathbf{x}_2 - \boldsymbol{\mu}_{2,i})}. \quad (5)$$

To acquire  $\boldsymbol{\mu}_{1,i}$ ,  $\boldsymbol{\mu}_{2,i}$ ,  $\Sigma_{11,i}$ ,  $\Sigma_{12,i}$ ,  $\Sigma_{21,i}$ , and  $\Sigma_{22,i}$ , the mean values and covariance matrices estimated with the EM algorithm were partitioned as

$$\boldsymbol{\mu}_i = \begin{pmatrix} \boldsymbol{\mu}_{1,i} \\ \boldsymbol{\mu}_{2,i} \end{pmatrix} \quad (6)$$

$$\Sigma_i = \begin{pmatrix} \Sigma_{11,i} & \Sigma_{12,i} \\ \Sigma_{21,i} & \Sigma_{22,i} \end{pmatrix}. \quad (7)$$

## II.G. Validation

The GMR model was validated using a LOOCV approach illustrated in Fig. 1. The model was estimated from the MR and CT data from four patients (training set) and applied to

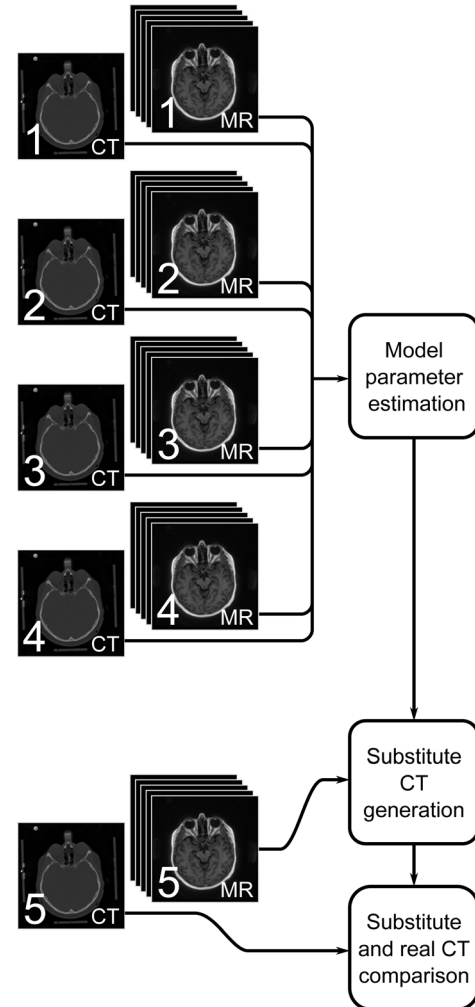


FIG. 1. One fold in the cross-validation procedure. CT and MR data from patients 1–4 and MR data from patient 5 were used to generate an s-CT for patient 5. The s-CT was then compared to the real CT of patient 5. In each fold, these steps were repeated but with patients 1–5 cyclically permuted.

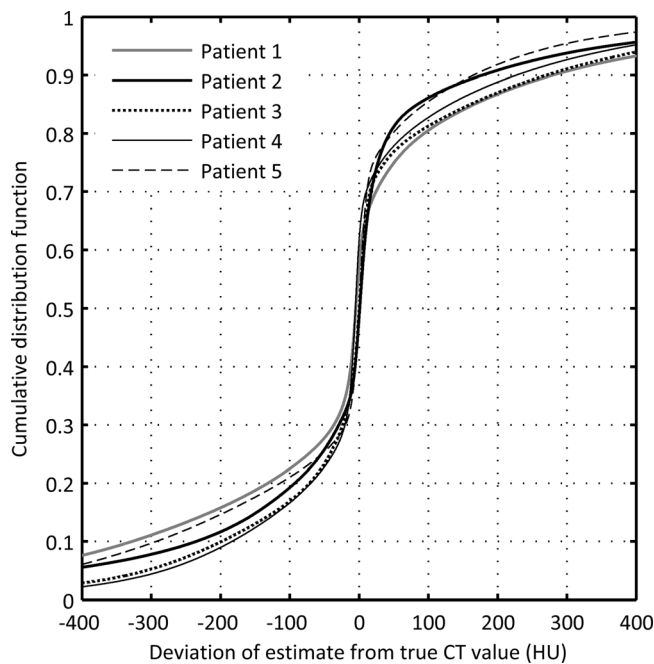


Fig. 2. Cumulative distributions of the deviation of the estimated CT number from the true CT number. The distribution for each of the five patients is shown. This curve shows what fraction of voxels for each patient that deviate less than a particular CT number.

the MR data of the remaining patient (validation set) to generate an s-CT image. This procedure was repeated for all five combinations of training and validation data. The s-CT was compared to the real CT for the validation set by calculating the mean absolute error (MAE) in HU for all voxels inside the binary mask.

Software to carry out the cross-validation procedure was developed in MATLAB. The software made use of the  $k$ -means and EM algorithms found in the Netlab toolbox.<sup>20</sup>

### III. RESULTS

The LOOCV MAE for the five patients was 137 HU. The MAE varied from 117 up to 176 HU for the individual patients. The cumulative distribution of HU deviations for each patient is seen in Fig. 2. The largest differences between CT and s-CT images were seen at the surface of the patients and at the bone–tissue and air–tissue interfaces inside the head (Fig. 3). Both MR and CT artifacts, which are not related to the GMR model, affect the results. The streak artifacts in Figs. 3(k) and 3(l) were the result of aliasing caused by the sampling pattern in the UTE sequence [vastly undersampled isotropic projection reconstruction (VIPR) (Ref. 21)] in combination with a high signal intensity outside the field of view. Streak artifacts seen in Figs. 3(a) and 3(c) originate from the reconstruction of the CT images and were caused by high density material in the fixation devices used. The deviations between CT and s-CT caused directly by the fixations, seen in the CT images in Fig. 3, were not included in calculating the MAE or in the cumulative error distributions shown in Fig. 2.

The relationship between the predicted and the real CT number is shown in Fig. 4 for patient 4. The lack of voxels

in the upper left and lower right corners of Fig. 4 shows that the model was able to accurately distinguish bone from air. The dominating errors were, as can be seen in Figs. 3 and 4, found at interfaces between the soft tissue and air and at interfaces between the soft tissue and bone. In Fig. 4, this is indicated by the wider peaks of histograms ii and iv compared to the peaks of histograms i, iii, and v.

Calculations were performed on a computer with an Intel Core i7 Processor. The full cross-validation procedure ran in 11 min. To generate all slices for an s-CT using pre-estimated parameter values required 110 s.

### IV. DISCUSSION

A method for generating a substitute CT image from MR images has been presented and then evaluated on the head regions of five patients using cross-validation. The presented method differed from earlier work<sup>7–9</sup> in that it used UTE MRI sequences with two different flip angles and Gaussian mixture regression to generate an s-CT rather than air, soft tissues, and bone segmentation converted to an attenuation map by bulk density assignments. The method prediction step was completely automatic with no manual delineation or threshold selection and resulted in high accuracy as illustrated in Figs. 2–4.

The streak artifacts present in the images from the UTE sequences become more severe when larger body parts, such as thorax and pelvis, are imaged. Therefore, the method has only been tested on the head and neck region. Reducing these artifacts for larger fields of view would be pivotal for making the method generally applicable.

Attenuation maps generated from an s-CT have more finely spaced attenuation levels than maps generated from segmentations as seen by the diagonal distribution of voxels in the joint histogram of Fig. 4(a). Instead of being combined, bone of different densities are assigned different attenuation coefficients, thus improving both attenuation correction and dose calculation when compared to segmentation based methods.

The largest deviations between real CT and s-CT images were located at the air–soft tissue and the bone–soft tissue interfaces where susceptibility effects cause a very short T2\*.

Some model generation and validation errors could be attributed to causes not directly related to the model. Such causes included streak artifact in CT and MR images, patient motion during scanning, changes in patient anatomy and position between scans, and uncertainties in image registration. Due to the small patient sample size, it is difficult to draw conclusions regarding the size of the contribution to the error from the different causes. However, the streaks up through the head in Fig. 3(l) and the deformation of the patient's cheeks in Fig. 3(c) suggest that artifacts and changes in patient anatomy are large contributors whereas the manual evaluation of the image registration suggests that registration induced uncertainties are small in the nondeformed parts of the head. Eliminating or reducing these effects should increase the accuracy and precision of the method even further.

While a particular set of MR images were used in this article, other sequences could have been used provided that



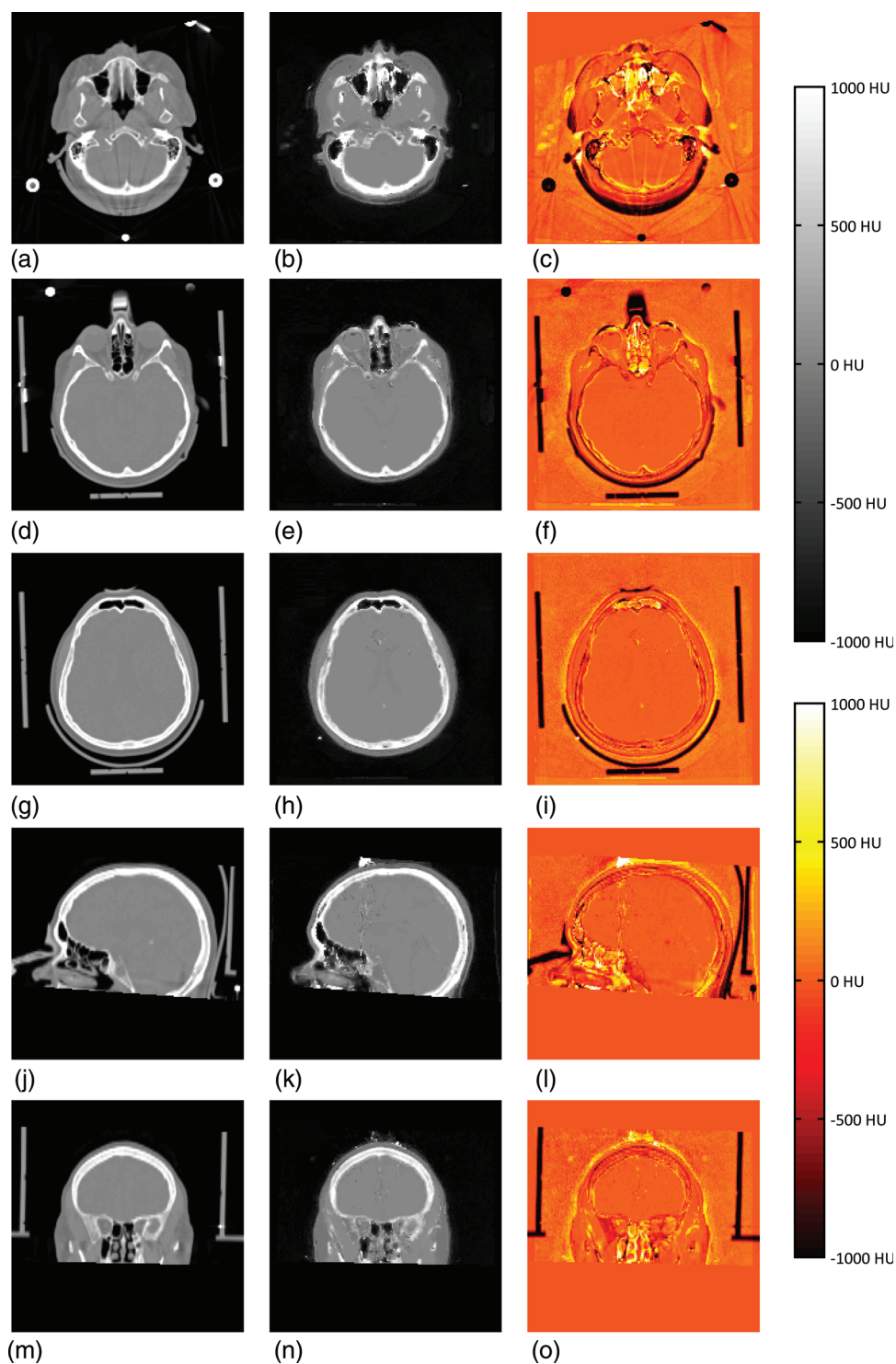


FIG. 3. Real CTs [(a), (d), (g), (j), (m)], s-CTs [(b), (e), (h), (k), (n)], and difference images [(c), (f), (i), (l), (o)] of patient 4. The first three rows show transverse slices, the fourth row a sagittal slice, and the fifth row a coronal slice. The upper scale bar belongs to the real and substitute CT whereas the lower belongs to the difference images. For the difference image, a yellow–white tone indicates a higher CT number in the s-CT compared to the real CT and a red–black tone the reversed.

their images showed sufficient contrast to distinguish between air, bone, and soft tissues. This is important since different institutions may have similar but not identical sequences available, such as a 2D UTE sequence with slice selection rather than a 3D UTE sequence. These sequences could generate slightly different image contrasts, which would

introduce bias if parameters estimated using one sequence set were used to generate an s-CT from another sequences set. Regression model parameter estimation could then be performed once per institution or once per manufacturer.

Generation of other MR images instead of s-CT images is also possible. Ideally, a larger set of images with different

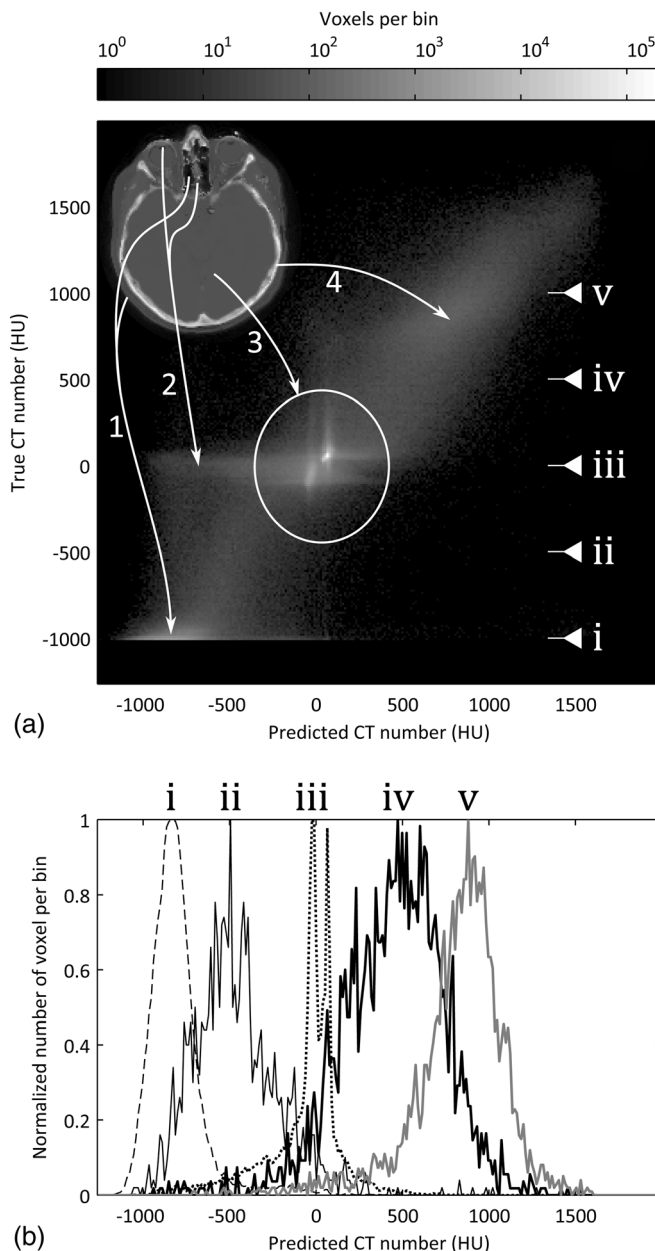


FIG. 4. (a) Joint histogram of the predicted CT number vs the true CT number for the voxels of patient 4. The bar at the top indicates the relationship between the number of voxels per histogram bin and the shade of gray in the pixels of the joint histogram. Arrows show where four different tissues classes appear in the joint histogram. Arrow 1: air, arrow 2: soft tissues with short T2\*, arrow 3: soft tissues, arrow 4: bone. Accurate discrimination between the air and the bone is seen by the lack of voxels in the upper left and lower right corners of the joint histogram. The roman numerals indicate five horizontal lines in the joint histogram that are shown as histograms in (b). Each of the histograms has been normalized to one for the peak value. These histograms show the spread of predicted CT numbers in the substitute CT for voxels with a true CT number of (i) -1000 HU, (ii) -500 HU, (iii) 0 HU, (iv) 500 HU, and (v) 1000 HU.

contrasts, possibly including an s-CT, could be generated from the images of a small set of sequences, thus reducing patient examination time. This approach is similar to that of synthetic MRI.<sup>22</sup>

Attenuation maps could also be derived directly from MR data rather than through an intermediate s-CT. Since a set of MR images has the potential to provide a more complete

description of tissue composition compared to a single CT image, the chemical composition and mass density maps derived from an MR could even surpass those derived from a CT, for example, in particle therapy.

For radiotherapy purposes, the extra sequences used for the formation of the s-CT are added to the scanning protocol for the radiotherapy planning. The images used for target definition will hence be acquired in the same imaging session as the s-CT sequences, which simplifies the registration process.

## V. CONCLUSIONS

A method for automatic generation of substitute CT images from a set of MR images has been presented. Evaluation of the method using datasets from the head and neck regions of five patients shows that the method accurately predicts the HU value, voxel by voxel, which could make the method an ideal solution for applications where both the HU and the geometry are important, such as in MR based radiotherapy and PET/MR applications.

## ACKNOWLEDGMENTS

The authors thank Siemens Healthcare for providing their prototype UTE sequence for this project. This work was supported by grants from the Cancer Research Foundation in Northern Sweden.

<sup>a)</sup> Author to whom correspondence should be addressed. Electronic mail: adam.johansson@radfys.umu.se.

<sup>1</sup>H.-P. W. Schlemmer, B. J. Pichler, M. Schmand, Z. Burbar, C. Michel, R. Ladebeck, K. Jattke, D. Townsend, C. Nahmias, P. K. Jacob, W.-D. Heiss, and C. D. Claussen, "Simultaneous MR/PET imaging of the human brain: Feasibility study1," *Radiology* **248**, 1028–1035 (2008).

<sup>2</sup>L. Chen, R. A. Price, Jr., L. Wang, J. Li, L. Qin, S. McNeeley, C. M. Ma, G. M. Freedman, and A. Pollack, "MRI-based treatment planning for radiotherapy: dosimetric verification for prostate IMRT," *Int. J. Radiat. Oncol., Biol., Phys.* **60**, 636–647 (2004).

<sup>3</sup>T. Boettger, T. Nyholm, M. Karlsson, C. Nunna, and J. C. Celi, "Radiation therapy planning and simulation with magnetic resonance images," *Proc. SPIE* **6918**, C9181–C9181 (2008).

<sup>4</sup>M. Karlsson, M. G. Karlsson, T. Nyholm, C. Amies, and B. Zackrisson, "Dedicated magnetic resonance Imaging in the Radiotherapy Clinic," *Int. J. Radiat. Oncol., Biol., Phys.* **74**, 644–651 (2009).

<sup>5</sup>T. Nyholm, M. Nyberg, M. Karlsson, and M. Karlsson, "Systematisation of spatial uncertainties for comparison between a MR and a CT-based radiotherapy workflow for prostate treatments," *Radiat. Oncol.* **4**, 54 (2009).

<sup>6</sup>J. Jonsson, M. Karlsson, M. Karlsson, and T. Nyholm, "Treatment planning using MRI data: an analysis of the dose calculation accuracy for different treatment regions," *Radiat. Oncol.* **5**, 62 (2010).

<sup>7</sup>V. Keereman, Y. Fierens, T. Broux, Y. De Deene, M. Lonneux, and S. Vandenberghe, "MRI-based attenuation correction for PET/MRI using ultrashort echo time sequences," *J. Nucl. Med.* **51**, 812–818 (2010).

<sup>8</sup>C. Catana, A. van der Kouwe, T. Benner, C. Michel, M. Hamm, M. Fenchel, B. Fischl, B. Rosen, M. Schmand, and A. Sorensen, "Toward implementing an MRI-based PET attenuation-correction method for neurologic studies on the MR-PET brain prototype," *J. Nucl. Med.* **51**, 1431–1438 (2010).

<sup>9</sup>M. Hofmann, F. Steinke, V. Scheel, G. Charpiat, J. Farquhar, P. Aschoff, M. Brady, B. Scholkopf, and B. J. Pichler, "MRI-based attenuation correction for PET/MRI: A novel approach combining pattern recognition and atlas registration," *J. Nucl. Med.* **49**, 1875–1883 (2008).

<sup>10</sup>M.-L. Montandon and H. Zaidi, "Atlas-guided non-uniform attenuation correction in cerebral 3D PET imaging," *NeuroImage* **25**, 278–286 (2005).

<sup>11</sup>H. Zaidi, M.-L. Montandon, and D. O. Slosman, "Magnetic resonance imaging-guided attenuation and scatter corrections in three-dimensional brain positron emission tomography," *Med. Phys.* **30**, 937–948 (2003).

- <sup>12</sup>M. Robson, P. Gatehouse, M. Bydder, and G. Bydder, "Magnetic resonance: An introduction to ultrashort TE (UTE) imaging," *J. Comput. Assist. Tomogr.* **27**, 825–846 (2003).
- <sup>13</sup>M. Robson and G. Bydder, "Clinical ultrashort echo time imaging of bone and other connective tissues," *NMR Biomed.* **19**, 765–780 (2006).
- <sup>14</sup>Z. Ghahramani and M. I. Jordan, "Supervised learning from incomplete data via an EM approach," in *Advances in Neural Information Processing Systems* (Morgan Kaufmann Publishers, Inc., San Francisco, CA, 1994), pp. 120–127.
- <sup>15</sup>M. Figueiredo, "On Gaussian radial basis function approximations: Interpretation, extensions, and learning strategies," *Proceedings of the 15th International Conference on Pattern Recognition*, Vol. 2 (IEEE Computer Society Press, Los Alamitos, CA, 2000), pp. 618–621.
- <sup>16</sup>S. Doran, L. Charles-Edwards, S. Reinsberg, and M. Leach, "A complete distortion correction for MR images: I. Gradient warp correction," *Phys. Med. Biol.* **50**, 1343–1361 (2005).
- <sup>17</sup>C. Karger, A. Hoss, R. Bendl, V. Canda, and L. Schad, "Accuracy of device-specific 2D and 3D image distortion correction algorithms for magnetic resonance imaging of the head provided by a manufacturer," *Phys. Med. Biol.* **51**, N253–N261 (2006).
- <sup>18</sup>T. S. Yoo, M. J. Ackerman, W. E. Lorensen, W. Schroeder, V. Chalana, S. Aylward, D. Metaxes, and R. Whitaker, *Medicine Meets Virtual Reality*, 2002 (unpublished).
- <sup>19</sup>N. Otsu, "A threshold selection method from gray-level histograms," *IEEE Trans. Syst., Man Cybern.* **9**, 62–66 (1979).
- <sup>20</sup>I. Nabney and C. Bishop, *Netlab Neural Network Software* (2004).
- <sup>21</sup>A. V. Barger, W. F. Block, Y. Toropov, T. M. Grist, and C. A. Mistretta, "Time-resolved contrast-enhanced imaging with isotropic resolution and broad coverage using an undersampled 3D projection trajectory," *Magn. Reson. Med.* **48**, 297–305 (2002).
- <sup>22</sup>J. B. Warntjes, O. D. Leinhard, J. West, and P. Lundberg, "Rapid magnetic resonance quantification on the brain: Optimization for clinical usage," *Magn. Reson. Med.* **60**, 320–329 (2008).